nature astronomy

Article

https://doi.org/10.1038/s41550-024-02412-7

Potential for observing geological diversity from mid-infrared spectra of rocky exoplanets

Received: 8 June 2023

Accepted: 10 October 2024

Published online: 14 November 2024

Check for updates

Emily C. First[1,2] ✉, Ishan Mishra[3,4], Esteban Gazel[1] ✉, Nikole K. Lewis[3], Jonathan Letai[1,5] & Leonard Hanssen[6]

The James Webb Space Telescope can potentially explore the geological diversity of the surfaces of rocky exoplanets, especially due to its access to mid-infrared wavelengths. Here we investigate the level of geological detail that it could be possible to observe with the low-resolution spectroscopy and photometric modes of the mid-infrared instrument onboard the James Webb Space Telescope. We used new emissivity measurements of 15 basaltic samples between 2 µm and 25 µm to produce synthetic spectra and photometric fluxes. We found that the mid-infrared instrument can, in principle, distinguish several specific mineralogical and bulk chemical signals among relatively similar rocks. In particular, hydrous minerals, such as amphibole and serpentine, which would signal the existence of past or present water, can have observable characteristics in both low-resolution spectroscopy observations (with the precision of 5 eclipses) and the integrated fluxes over mid-infrared instrument filter bandwidths (20–100 eclipses). Photometric fluxes are also sensitive to bulk compositions (for example, wt% Al_2O_3), which reflect magmatic processes. Our work demonstrates the potential for the James Webb Space Telescope and future observatories to access a fuller picture of exoplanet surface geology.

The James Webb Space Telescope (JWST) can potentially explore the composition and geological diversity of the surfaces of rocky exoplanets, especially due to its mid-infrared (MIR, 2.5–25 µm) capabilities, which are more extensive than those of any previous space-borne observatory. Composition measurements of the rocky surfaces of terrestrial planets, both in the Solar System and beyond, provide key information about how these planets formed and evolved[1–6]. Small, rocky exoplanets without lava oceans ($R < 1.6\ R_\oplus$ and $M < 2\ M_\oplus$) that orbit close to their host stars probably possess little to no present-day atmosphere[6–10], giving observers a clear view of their surfaces. The warm surfaces of these exoplanets glow at infrared wavelengths, providing us with an opportunity to measure light emitted directly from the planetary surface, as demonstrated with both Spitzer and JWST[6–8,11].

MIR characterization of the surface emission from temperate to warm ($T \lesssim 1{,}000$ K) terrestrial exoplanets orbiting M-dwarf stars, using facilities like the mid-infrared instrument (MIRI) onboard JWST, is optimal for two reasons. First, M-dwarf stars are smaller and cooler than Sun-like stars, making them ideal targets for detecting and observing close-in rocky exoplanets. Such systems maximize both the relative planet-to-star radius ratio and the ratio of the planetary flux to the stellar flux (F_p/F_*). The F_p/F_* signal from close-in terrestrial exoplanets[12] peaks (~1,000 ppm) at MIR wavelengths and then falls to well

[1]Department of Earth and Atmospheric Sciences, Cornell University, Ithaca, NY, USA. [2]Department of Geology, Macalester College, Saint Paul, MN, USA. [3]Department of Astronomy and Carl Sagan Institute, Cornell University, Ithaca, NY, USA. [4]Jet Propulsion Laboratory, California Institute of Technology, Pasadena, CA, USA. [5]Department of Physics, Northeastern University, Boston, MA, USA. [6]National Institute of Standards and Technology, Gaithersburg, MD, USA. ✉e-mail: efirst@macalester.edu; egazel@cornell.edu

https://doi.org/10.1038/s41550-024-02412-7

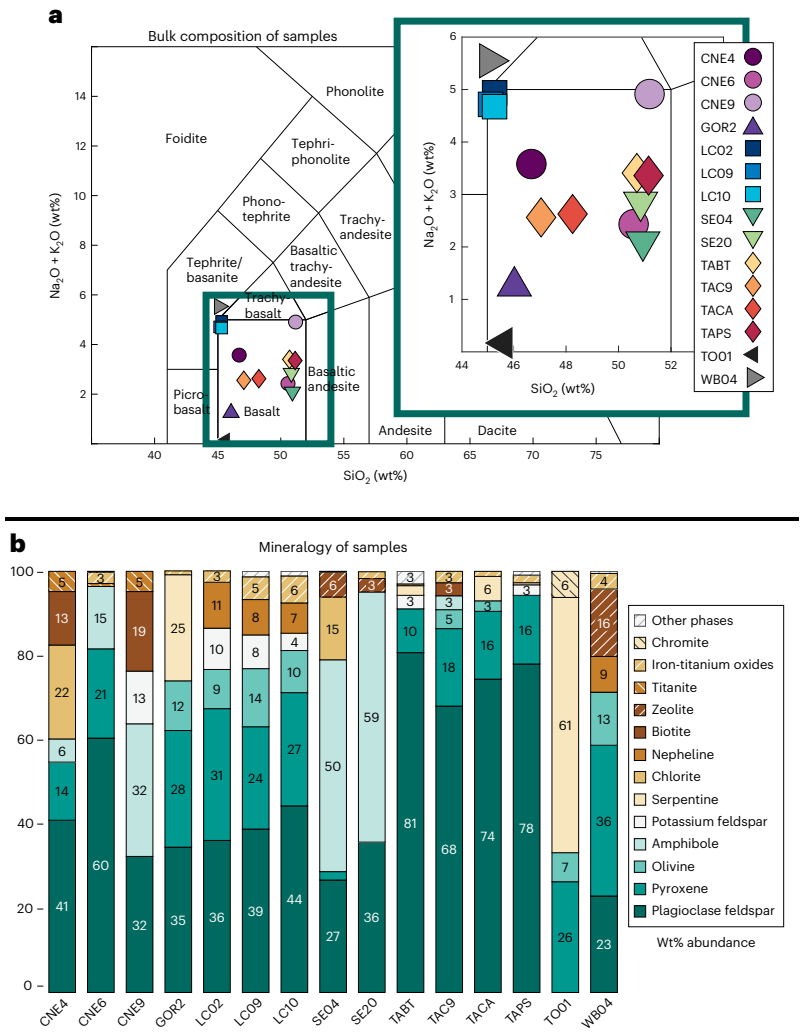

Fig. 1 | Geological sample characterization. a, Bulk chemistry of samples used in this study, plotted on a diagram of total alkali content ($Na_2O + K_2O$) versus SiO_2. All samples but one fall within the basalt field, with WB04 just across the line in the basanite field. Samples are grouped by locality, with rocks from the same locality assigned the same symbol shape. Circles, Coastal New England; upward triangle, Gorgona; squares, Lunar Crater; downward triangles, Santa Elena; diamonds, Talamanca; leftward triangle, Tortugal; rightward triangle, Ward's Science. **b**, Mineralogy of the samples plotted in **a** by phase wt%.

below 1 ppm ($F_p/F_* < 10^{-6}$) at wavelengths typically used to characterize reflected light from Solar System objects (for example, the ~1 µm band indicative of olivine abundance and composition[13,14]). Although future observatories (for example, the Habitable Worlds Observatory) should allow us to access the necessary visible and near-infrared (0.5–2.5 µm) F_p/F_* ratios, such measurements are beyond the capabilities of current facilities. Second, the chief rock-forming minerals are silicates, which have diagnostic vibrational features at MIR wavelengths, especially near 10 µm (refs. 15,16). Rock types (for example, basalt versus granite) can already be distinguished by their MIR spectra[12,17], so we focus on variations within a single ubiquitous rock type: basalt. Using both fresh and altered basaltic samples, we examined the potential for distinguishing features within a broadly similar suite of rocks.

Basaltic magmas form by partial melting of an ultramafic (SiO_2 < 45 wt% and MgO ≈ 40 wt%) silicate mantle[18,19]. Magma production is followed by crystallization and mixing processes, culminating with eruption onto a planetary surface or cooling in the shallow subsurface to produce the solid rock, basalt. After solidification, exposure to heightened temperature, pressure or circulating fluids can alter the chemistry and primary mineralogy of a basalt.

Basaltic rocks are defined according to different criteria, from mineralogy and texture to bulk chemistry[20]. They are the most abundant volcanic rocks on Earth, the Moon and Mars (Supplementary Fig. 1). They contain low SiO_2 (45–52 wt%) and high MgO (typically 5–15 wt%) relative to other crustal rocks, with a mineral suite that typically includes olivine ± pyroxene ± plagioclase feldspar. Basalts are expected to have a similarly large presence outside our Solar System, because modelling of bulk silicate planet compositions based on stellar chemistry implies that most planets around FGMK stars have mantles composed of olivine, orthopyroxene and clinopyroxene[21]. Regardless of the variation in proportion, mantle rocks composed of these minerals typically melt to produce basaltic magmas[18]. Although the spectra of some polluted white dwarfs (stellar remnants with accreted planetary debris) hint at exotic mantle mineralogies, others are consistent with this olivine–pyroxene mantle paradigm[22]. Moreover, thermal emission data from several rocky exoplanet surfaces are consistent with basalt (LHS 3844b (ref. 6) and GJ 1252b (ref. 11) from Spitzer 4.5 µm flux data; TRAPPIST-1 b (ref. 7) and TRAPPIST-1 c (ref. 8) from JWST's MIRI F1500W filter). This agreement between expectation and observation motivates our study to go beyond simple 'basalt' to examine what details of composition and mineralogy could be teased apart in the next generation of exoplanet characterization observations. These details are indicative of fundamental planetary processes, as reflected in our sample set.

https://doi.org/10.1038/s41550-024-02412-7

The basaltic rocks considered here represent three main melting processes related to plate tectonics on Earth. Although it is not our goal to link spectroscopic features to specific tectonic settings, we include variety in our sample set to provide context for the potential diversity of rocky worlds. At mid-ocean ridges, melting is triggered by the decompression of mantle material due to upwelling at the boundary of two diverging tectonic plates. Following eruption, basalts are altered by the circulation of hydrothermal fluids in the sea floor. Samples SE04 and SE20 are altered basaltic dikes from the Santa Elena ophiolite, Costa Rica, and represent this mid-ocean ridge setting[23]. At volcanic arcs (chains of volcanoes at the boundaries of tectonic plates), this hydrated ocean crust de-volatilizes as it subducts underneath another tectonic plate. The addition of volatiles to the overlying mantle initiates magma production. Arc basalts are sensitive to the make-up of these hydrous primary fluids[24]. Samples TABT, TAC9, TACA and TAPS are from the Talamanca Cordillera, a volcanic arc in Costa Rica[25–27]. Finally, some melting can occur due to hot thermal anomalies (plumes) originating in the deep mantle or associated with the break-up of supercontinents. In our sample set, LC02, LC09 and LC10 (Lunar Crater, Nevada[28]), TO01 (Tortugal, Costa Rica[29]) and GOR2 (Gorgona Island, Colombia[30]) are plume-related basalts. Samples CNE4, CNE6 and CNE9 are associated with the break-up of supercontinent Pangea[31,32]. This context of planetary processes is integral to gaining a better understanding of exoplanet surface compositions.

Here, we present a self-consistent analytical and modelling framework based on 15 terrestrial basalt samples from seven localities and different tectonic settings (Supplementary Table 1) to assess what spectral patterns and features might be discernible in JWST MIRI observations of exoplanet surfaces. Given the global scale of exoplanet observations, analyses of rocks, rather than individual minerals[12,33,34], brings us closer to the geological complexity of planetary surfaces. Although many spectral studies have focused on powdered material analogous to planetary regolith[16,33–35], we opted to analyse flat, solid samples so as to better understand the effects of compositional and mineralogical variations, without complications from surface roughness[36] and grain-size variability[37]. Although others have measured the MIR spectra of basalts (for example, refs. 17,38,39), our study examines how variation within this single rock type could manifest in exoplanet surface-emission observations. Thus, we focus on seeing first-principles mineralogical and compositional effects, necessarily simplifying other surface aspects that could complicate the analysis of observational data (for example, roughness and grain size). Although this approach yielded relatively high signals and optimistic model observations, it also highlights the importance and potential of using the full complement of JWST and future observatories' MIR tools to explore exoplanet geology, as well as the need for future laboratory work and modelling of a wide range of surface compositions and conditions. Choosing to analyse the spectra of solid materials is not without precedent[17,38–41]. Telescope observations have not yet constrained the physical nature of rocky exoplanetary surfaces, which could consist of regolith, solid outcroppings or both. Many processes, such as impacts and space weathering, are conducive to regolith formation on airless bodies. Although they are not an exhaustive reckoning of all possible surface variations, our results demonstrate how geologic variation might be observable among potential exoplanetary surfaces that until now have been grouped under the umbrella term 'basaltic'. Furthermore, regolith development is not instantaneous, as it forms at rates of about 1–5 mm per million years using Earth's moon as a proxy[42]. If a rocky exoplanet is young, had an atmosphere that was later lost[43,44] or hosts active volcanism, then its surface should include regions of intact rock.

Using a gold-coated integrating sphere and a MIR Fourier-transform infrared spectrometer, we acquired directional hemispherical reflectance (r_h) spectra of rock slabs that had been polished identically to eliminate the effects of surface roughness[36]. Mineral

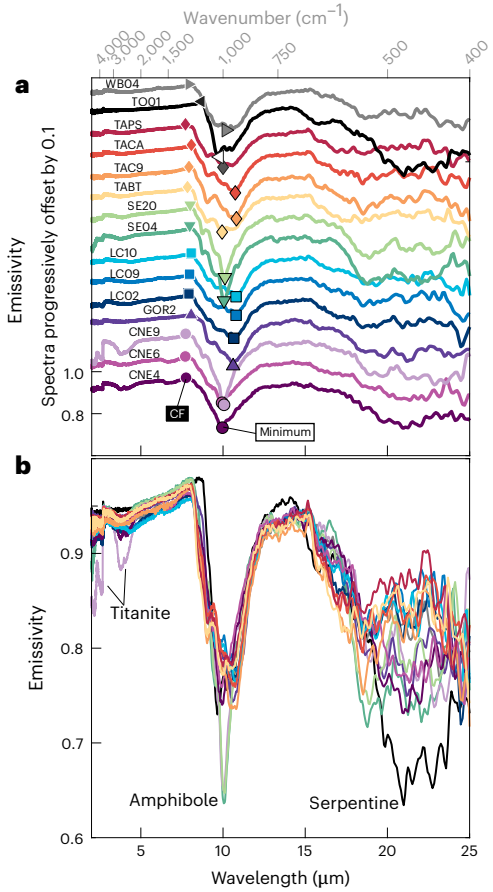

Fig. 2 | Laboratory-derived emissivity spectra. a, Spectrum of CNE4 plotted without adjustment. The other spectra are progressively offset by 0.1 vertical units. Symbols outlined in white pinpoint the maximum emissivity, or CF, for each sample. Symbols outlined in black mark the minimum emissivity (in the 8–12 μm range) for each spectrum. Samples from the same locality have the same symbol shape. **b**, All 15 spectra from the upper plot, with no offsets. Labels indicate the spectral features of the named mineral. Colours as in **a**.

proportions were determined with X-ray diffraction (XRD), and bulk chemistry was determined with X-ray fluorescence (XRF). MIR spectra were transformed to emissivity (ϵ) using Kirchhoff's law ($\epsilon = 1 - r_h$). See Methods for details of the measurements and uncertainties. Our set-up is suited well to considering disk-integrated observations of terrestrial exoplanets, as it allows the analysis of relatively large areas (~2 cm diameter) of multicomponent, natural-texture rocks. Emissivity data were used to directly model planetary emission, in contrast to previous efforts[12,45] that have used emissivity data and extensive calculations based on the Hapke model[46] (Methods).

Results

The 15 rock samples analysed are fully crystalline (Supplementary Fig. 2) and fall within or immediately adjacent to the basalt field of the total alkali–silica diagram (Fig. 1 and Supplementary Table 2). This plot is used to name and study volcanic rocks (those erupted and cooled on a planetary surface) based on their bulk chemistry. We use it here to constrain our sample selection and to acknowledge that in other contexts, different rock names could apply to some samples. Among these basaltic samples, mineral proportions vary but are generally similar among samples from the same locality (for example, LC02, LC09 and LC10). With the exception of TO01, the majority of each sample is composed of four minerals: plagioclase feldspar, (clino)pyroxene, olivine and amphibole, a hydrous inosilicate mineral (Fig. 1 and Supplementary Table 3). The remainder of each sample comprises a variety

https://doi.org/10.1038/s41550-024-02412-7

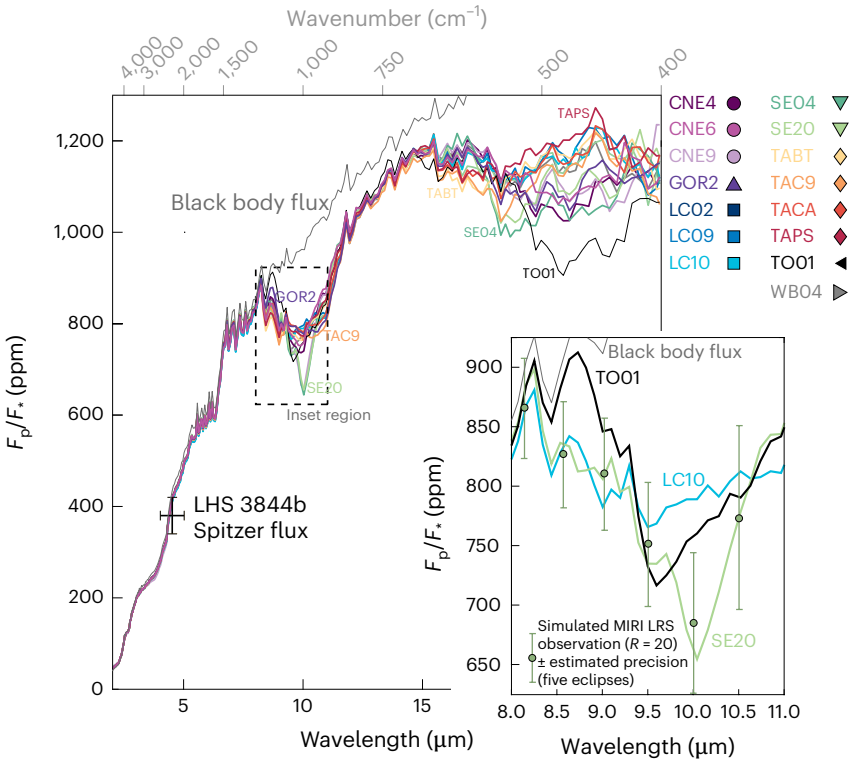

Fig. 3 | Modelled planet-to-star fluxes. The 15 F_p/F_* simulations shown assume an airless, rocky exoplanet with a homogeneous surface temperature and a surface composition equivalent to each laboratory-measured rock sample in this study. R = 100. The PHOENIX stellar model of red dwarf LHS 3844 and the planetary parameters of its close-in rocky planet LHS 3844b were used as a representative star–planet system. The black body curve was calculated using the LHS 3844 PHOENIX stellar model and a planetary black body. Inset, Magnification of the F_p/F_* models for three representative samples: relatively fresh, unaltered basalt LC10; amphibole-rich sample SE20; and serpentinized sample TO01. Dots are simulated MIRI LRS observations of a surface composed of sample SE20. High and low error bars show the estimated observation precision, assuming five eclipse observations of a planet like LHS 3844b, binned to R = 20 (Methods). The LRS simulation highlights the expected spectral deviation among the three basaltic samples near 10 μm. Symbols at top right are a reminder of which samples come from the same locality (as indicated by the symbol shape). The 15 modelled flux line colours correspond to symbol colours.

of primary minerals grown from the magma along with secondary, or alteration, minerals that have replaced primary minerals due to exposure to near-surface conditions, including circulating fluids and submagmatic temperatures. Sample TO01 is 61 wt% serpentine, a phyllosilicate mineral containing structural water, that is, hydroxyl groups in the crystal lattice.

In laboratory data, all samples have broadly similar MIR spectra, with the average sample emissivity (2–25 μm) ranging from 0.84 to 0.88 (Fig. 2a,b and Supplementary Table 4). Complex multi-trough features near 10 μm are due to the reststrahlen bands (fundamental Si–O bond vibrations) of the silicate minerals (chiefly olivine, pyroxene, plagioclase, amphibole and serpentine; Supplementary Fig. 3). Samples with a high plagioclase content (for example, TABT, TAC9, TACA and TAPS) have high emissivity in the further MIR range (~20–25 μm). Samples containing titanite have sharp minima near 2.5 and 4.0 μm. Samples containing >30 wt% amphibole have deep emissivity minima between 10.0 and 10.1 μm. The three samples with >5 wt% serpentine have the three longest-wavelength emissivity maxima (Christiansen features, CFs) of the sample set (Fig. 2a and Supplementary Table 4). Sample TO01, with 61 wt% serpentine, has the longest CF wavelength measured (8.54 μm) and has the lowest average emissivity over the 2–25 μm range (Supplementary Table 4).

When these laboratory data were input to a planetary flux model using the star + planet system LHS 3844 (ref. 6) as a basis (Methods), the F_p/F_* ratios recovered show similar features (Fig. 3). The most notable difference is that spectral features below ~8 μm are overwhelmed by the stellar flux. However, above this wavelength, the key features noted in laboratory emissivity spectra are visibly present.

The integrated model flux over MIRI photometric filter bandwidths (Methods) also reveals patterns with mineral content and rock composition (Fig. 4 and Supplementary Tables 5 and 6). Samples with the highest amphibole contents (>30 wt%) stand out from the rest of the sample set using the F770W and F1000W filters (Fig. 4a). All four samples containing serpentine (>0.5 wt% by XRD) fall within a narrow range of flux values using the F1800W filter and the F1800W − F770W difference (Fig. 4b). Finally, the alumina (Al_2O_3) content of basaltic samples tracks the simulated F2100W MIRI band-pass flux and the F1500W − F2100W flux difference (Fig. 4c). If a sample contains serpentine, the serpentine content is negatively correlated with Al_2O_3 (Fig. 4c). The alumina content is positively correlated with the plagioclase feldspar content (Fig. 1 and Supplementary Table 7). Other mineralogical and bulk compositional parameters (for example, wt% MgO) correlate with other photometric band-pass fluxes (Supplementary Table 7).

Discussion

JWST simulations

Our spectral measurements show distinctive features that reflect the mineralogy of our samples. Here, we assess the extent to which the features in laboratory spectra and theoretical noise-free high-resolution ($R \approx 2{,}500$) models will be discernible within the precision limits and spectral resolution of time-series observation modes available with JWST MIRI. To that end, we used the PandExo simulation environment[47] to estimate the precision of observations at different spectral resolutions (R) and numbers of eclipses, within the MIRI low-resolution spectroscopy (LRS) range (~5–12 μm), using LHS 3844 system parameters

https://doi.org/10.1038/s41550-024-02412-7

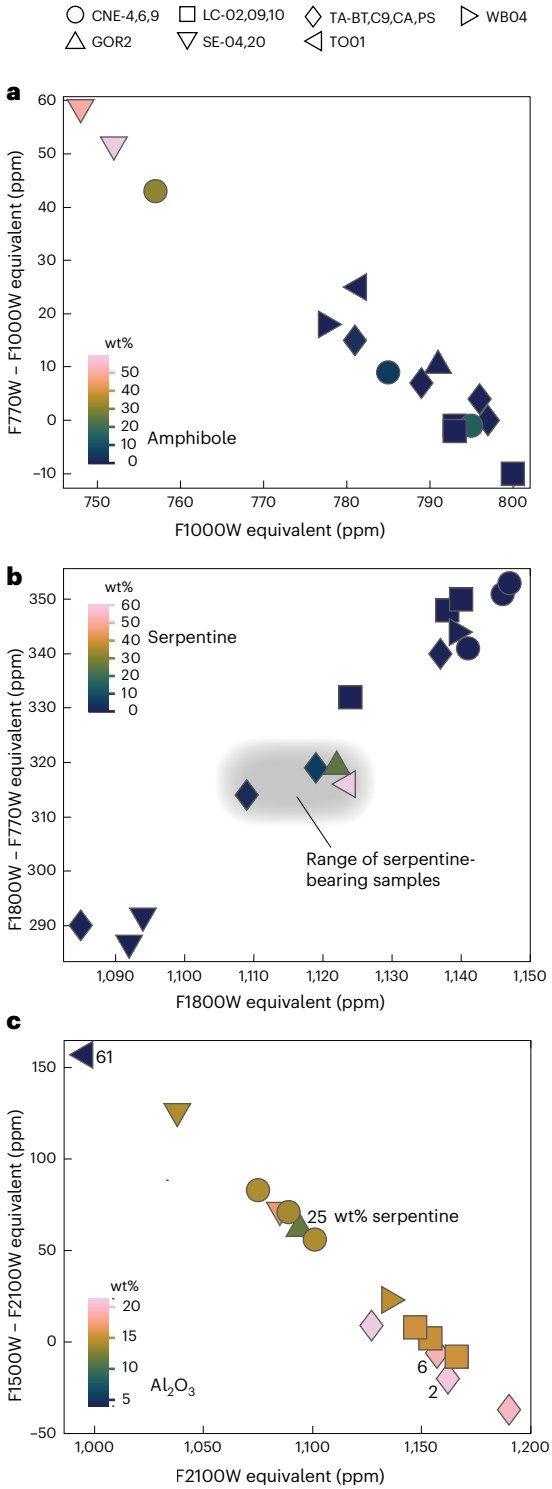

Fig. 4 | Simulated MIRI broadband fluxes. a–**c**, Symbol shapes correspond to locality, and symbol colour is indicative of amphibole content (**a**), serpentine content (**b**) and alumina content (**c**). In **b**, the shaded area includes all samples that contain serpentine at >0.5 wt% levels. In **c**, the serpentine-bearing samples are annotated with their serpentine abundance in wt%. Approximately 20–30 eclipse observations with JWST MIRI photometric mode would be needed to achieve the precision necessary to characterize basaltic surfaces in terms of amphibole (~20 ppm), and 50–100 eclipses to access signals from serpentine (~20 ppm) or alumina (~50 ppm), using the LHS 3844 system parameters as a basis.

and assuming an airless planet. The LHS 3844 system is used as our model basis because it provides parameters for an M-dwarf star orbited closely by a rocky planet[6]. However, the goal of our study is not to assess planet LHS 3844b specifically, but rather to consider the wide plausible range of basaltic rocky exoplanets that will be observed in the coming years.

We selected TO01, SE20 and LC10 as examples of altered serpentine-rich, amphibole-rich and relatively unaltered basalt, respectively. At $R = 20$ and the precision of five eclipses, key spectral features near 10 µm stand out in simulated JWST MIRI LRS time-series observations (Fig. 3). The sharp minimum for SE20 is ~125 ppm deep, sufficient to be measured with the exhibited precision (±50–60 ppm). The maximum flux for TO01 (an estimate of its CF at this spectral resolution) has a similar spectral contrast and occurs at 8.73 µm, which is ~0.5 µm higher than the SE20 and LC10 maxima (8.25 µm). Thus, this feature should also be measurable. The SE20 10 µm feature is driven by the abundance of amphibole (59 wt%), a mineral containing structural water (OH). Reststrahlen features of olivine and serpentine are also relatively sharp (Supplementary Fig. 3) but are offset from that of amphibole by ~0.5 µm, which is sufficient to differentiate these minerals at the modelled resolution ($R = 20$; Fig. 3, inset). An amphibole signal could point to a rocky surface that underwent substantial alteration by medium-grade metamorphic processes and fluid circulation (for example, amphibolite facies, ~0.3–1.1 GPa and ~500–700 °C)[48]. The offset wavelength and high flux for the CF of sample TO01 are driven by its high serpentine content. Sample GOR2, which contains the second-most serpentine, has the second-highest flux at 8.73 µm, consistent with serpentine driving the signal. Serpentine forms by a process known as serpentinization, which involves the relatively low-temperature (≲400 °C) hydration of nominally anhydrous primary phases, like olivine and pyroxene, at or near planetary surfaces[49]. A comparable spectral signature would thus be indicative of surface water (past or present) and relatively low surface temperatures (≲400 °C) on an exoplanet. On the other hand, sample LC10, the more typical, unaltered basalt, lacks the spectral features of the heavily altered samples with hydrous phases and, more consistent with ref. 45, is unlikely to be differentiable from other relatively pristine rocks of basaltic composition in MIRI LRS time-series observations.

Combinations of JWST MIRI filters are also sensitive to mineralogical and bulk chemical characteristics of basaltic rocks, including high concentrations of amphibole (Fig. 4a), the presence of serpentine (Fig. 4b) and the amount of Al_2O_3 (Fig. 4c). Both serpentine and amphibole are hydrous minerals that indicate some exposure to water. To distinguish basaltic planetary surfaces rich in these materials would require ~20 ppm precision for each filter and filter combination indicated (Fig. 4a,b). An ~50 ppm precision could distinguish 25 wt% from 15 wt% from 5 wt% Al_2O_3 (Fig. 4c). Like other chemical parameters, the bulk Al_2O_3 content of a basaltic surface would reflect the mineralogy, depth or melting extent of its mantle source[18]. Using the JWST exposure time calculator with LHS 3844 system parameters, we estimated that 20–30 eclipses would be necessary to distinguish an amphibole-rich surface whereas 50–100 eclipses would be necessary to distinguish a surface with serpentine or to estimate the bulk alumina content (Fig. 4 and Supplementary Table 6).

Although using MIRI broadband filters to assess basalt mineralogy or bulk chemistry would require considerable JWST observing time, the JWST MIRI detection of Earth-like levels of ozone (O_3) on the TRAPPIST-1 planets would require a comparable commitment (30–60 transit measurements[50]). The detailed surface characterization of rocky exoplanets is conceivable; it simply requires a target promising enough for the investment. When planning new instrument development and observation strategies, it should also be remembered that our study examines variation within this single rock type, basalt, thus exploring the far reaches of the potential of JWST. Broadband flux measurements of different rock types (for example, basaltic and granitic) would probably yield differences in mineral and chemical parameters that would be apparent at lower precision.

Interpreting linked parameters

Mineral abundance is not an isolated quantity. The amount of any given mineral in a rock affects and is affected by the formation of other minerals, which are all linked to the bulk chemical composition of the rock. Although potentially complex, these dependencies do not necessarily prevent the recognition of signatures from specific minerals. For example, the samples with the most amphibole are the samples with the least clinopyroxene (SE20, SE04 and CNE9), because the two minerals share many of the same major chemical components. However, only amphibole requires volatiles (OH, Cl and F) in its structure. Thus, pyroxene tends to form under drier conditions and amphibole in fluid-bearing environments[51].

For samples that contain serpentine, there is a positive, linear correlation between serpentine and bulk rock MgO content and a negative, linear correlation between serpentine and bulk Al_2O_3 as well as plagioclase content (Fig. 4c and Supplementary Fig. 4). However, the distinct flux range occupied by the serpentine-bearing samples in Fig. 4b has no relation to the presence or abundance of any other mineral or chemical parameter, suggesting that serpentine is the true driver of that signature. Likewise, the CFs in our sample set (Fig. 2a and Supplementary Table 4) are not correlated with MgO, Al_2O_3 or plagioclase content, meaning that the longer-wavelength CFs of serpentine-bearing samples are attributable to that mineral. Thus, our data demonstrate unique correlations of mineralogy with simulated JWST spectra, and they point to ways in which dependent variables provide further insight. For example, if serpentine presence were inferred from MIRI LRS spectra or the F1800W and F770W filters, then proxies like bulk Al_2O_3 (using the F1500W and F2100W filters) could be used to estimate its abundance.

JWST MIRI simulations of a large array of rock samples linked to mineralogy and bulk composition will be critical for future exoplanet observation planning and subsequent characterization, which would allow us to fully explore the potential complexities of rocky exoplanet surfaces. Variables like surface roughness, grain size, space weathering and atmospheric effects should be considered as models progress. For example, smaller grain size could shift the CF of rocks and minerals to longer wavelengths[17,37,52] and lessen the spectral contrast in the reststrahlen region[37,52], changes that could mean higher precisions would be needed to distinguish features in Figs. 3 and 4. These factors are important to consider for regolith-dominated surfaces, whereas more direct application of our data is logical for young or volcanically active planets.

Implications

Both MIRI LRS and the photometric band-pass filters show promise for assessing the broad mineralogical content of basaltic rocks, keeping in mind that to address first-principles mineralogical and compositional effects, our dataset omits other complexities (for example, rough or regolith surfaces). The MIRI LRS spectral range (5–12 μm) is particularly useful for distinguishing basaltic surfaces with high contents of minerals formed by alteration or metamorphism, whereas photometry has the potential to distinguish these as well as other mineralogical and bulk compositional features. Especially critical are minerals that host volatiles in their structures, such as amphibole and serpentine. However, we make no claims as to the composition of LHS 3844b specifically.

Amphibole contains OH, F or Cl and can form due to metamorphism and fluid-induced alteration of basalts and ultramafic rocks[51]. This incorporation of fluids then influences magmatic processes at volcanic arcs, where amphibole is a common primary mineral phase in more evolved magmas (for example, andesites and dacites). There would probably have to be large amounts of amphibole (~30 wt%) on the surface of a rocky exoplanet for detection, but it does form on planetary bodies beyond Earth, and some types of amphibole are stable above 900 °C (1,173 K) (for example, ref. 53). Small amounts of primary (magmatic) amphibole occur in meteorites from Mars[54], and secondary amphibole has been detected in ordinary chondrites[55].

In the presence of water and at low temperatures relative to melt formation, olivine and pyroxene react to form serpentine[49,56]. The process by which these primary minerals are converted to serpentine reflects the near-surface environment of a planet. Serpentinization also increases rock volume and releases H_2 gas, leading to abiotic CH_4 production in the presence of CO_2 (ref. 49). Such gases could affect atmospheric retrievals. Heavily serpentinized basalts exhibit several unique features, making them potentially distinguishable with both MIRI LRS data (Fig. 3 inset) and photometry. In particular, the F1800W filter fluxes and the flux differences between the F770W and F1800W filters show a distinct cluster of serpentine-bearing samples (Fig. 4b). One complication is that the stability of serpentine limits detections to surface temperatures $\lesssim$400 °C ($\lesssim$673 K), but cooler surfaces have a lower flux. Critically, however, finding a serpentine signature does not require observing a planet in the possibly brief time window during which it contains liquid water. There are clay and serpentine minerals on the surface of Mars today[1,57], even though the planet is last thought to have had surface water more than two billion years ago[58]. Thus, were JWST observations to capture a planetary serpentine signature, the planet has or previously had liquid water at its surface and probably has a temperature of $\lesssim$400 °C.

We have shown that the power of JWST and future observatories need not be limited to broad rock type distinctions for rocky exoplanet surfaces, many of which are expected to be basaltic. With dedicated observing investment, a combination of spectroscopy and multi-filter photometry could reveal bulk compositional parameters (for example, Al_2O_3) and the presence of certain minerals (for example, serpentine) on these basaltic surfaces. In MIRI LRS and photometric simulations, the features that stand out the most are those of water-bearing minerals that form due to the alteration of basalts by metamorphism and circulating fluids. Thus, future observations of basaltic rocky exoplanets have the potential to reveal geological details that reflect not only primary magmatic processes but also secondary alteration in the presence of water.

Methods

Geological samples

The 15 specimens used in this work were all collected or obtained before the conception of this project. For this work, we selected them from the research collection of author E. Gazel at Cornell University. One sample was previously purchased from Ward's Science (WB04). Of the remaining 14 samples, three were collected from public areas along the southern coast of Maine, USA, in 2015 (CNE4, CNE6 and CNE9). Three were collected from Lunar Crater, Nevada, USA, in 2010 (LC02, LC09 and LC10). One was collected on Gorgona Island, Colombia, in 2019 (GOR2). Seven were collected from localities in Costa Rica, in 2006 (Talamanca, TABT, TAC9, TACA and TAPS), 2011 (Santa Elena, SE04 and SE20) and 2014 (Tortugal, TO01). All samples were legally collected, and if necessary, properly permitted and exported according to the laws of their country of origin.

Laboratory analyses

Fourier-transform infrared spectroscopy. We acquired directional hemispherical reflectance (r_h) spectra from 368 to 7,498 cm^{-1} (1.3–27 μm) for 15 samples, at a resolution of 4 cm^{-1}, using a Bruker Vertex 80 Fourier-transform infrared spectrometer equipped with an A 562-G gold-coated integrating sphere and OPUS (v.8.5.29) spectral processing software, at the Department of Earth and Atmospheric Sciences, Cornell University. A globar MIR source and a KBr beam splitter were used. Reference measurements were acquired on the inner surface of the gold cap of the upper sphere port, before loading samples. Flat, polished rock slabs were placed in the upper sphere port, using the sample holder. The sphere was purged with dry air to lessen the interference of atmospheric H_2O and CO_2. Any remaining features were removed using the atmospheric compensation algorithm in OPUS.

Each reflectance spectrum consists of 358 co-added scans, acquired at a sampling rate of 2.5 kHz using a DLaTGS room-temperature detector. During each measurement session, a diffuse gold disk, D25A18, was measured using the same set-up and acquisition parameters as the samples. This disk is a standard-quality sample from the National Institute of Standards and Technology (NIST), part of a set used previously to assess and correct MIR integrating sphere measurements[59]. Raw data for the rock samples and D25A18 are provided as csv files in the Supplementary Information.

Repeat analyses of D25A18 are one indicator of analytical precision. We calculated mean D25A18 reflectance values by resampling the spectra to 100 points per micrometre using an evenly spaced linear interpolation and taking the average of these values over the indicated wavelengths. Cornell reflectance values for D25A18, averaged over 2–14 µm, are within 0.8% relative of each other. The average reflectance values over 14–25 µm are within 2.2% of each other. Within the latter range, looking specifically at the noisiest, longest-wavelength values, the average reflectance values over 20–25 µm are within 2.9% relative for all four Cornell analyses. The Cornell D25A18 samples, averaged over the longest-wavelength MIRI filter used in this contribution (F2100W, 18.5–23.5 µm), differ by no more than 1.9% relative. For the NIST data across the spectral range up to 18.5 µm, the expanded uncertainty (95% confidence interval) is ±3% relative to the value. Thus, the Cornell data have reasonable precision even at wavelengths beyond where NIST standard data exist. The data are noisier at longer wavelengths, but our conclusions draw upon integrated fluxes at those wavelengths, not specific peaks, so the reproducibility of the average reflectance values here is a good measure of analytical precision for our purposes.

The Cornell data display lower emissivity (by 2–3%) than the NIST measurement of D25A18 (Supplementary Fig. 5). Applying a normalization factor to our rock spectra based on the ratio of our D25A18 measurements to the NIST measurement of D25A18 (as done in ref. 59) resulted in an absolute difference of 0.0013–0.0020 in average emissivity of the rock samples between 2 and 14 µm (the range of NIST data). This equates to a 0.15% to 0.22% difference relative to the original spectra (CNE9 is shown as an example in Supplementary Fig. 6). Given that this change is roughly two orders of magnitude smaller than any features of interest to JWST, we opted to keep all spectra in their initial form and no normalization factor was applied.

Analysing the signal obtained by measuring a light trap (which would ideally reflect 0% of incoming light) is another means of assessing the uncertainty of spectral observations. In our case, light trap measurements using the same detector, light source and set-up geometry as the rock samples gave reflectance values just above 0.02 before increasing at wavelengths longward of ~15 µm (Supplementary Fig. 7). The longest-wavelength data we used to draw any quantitative conclusions are the F2100W band-pass data (18.5–23.5 µm). Over this range, the light trap averaged a reflectance of 0.049. Mean values were calculated as described above for D25A18. For the F1800W band-pass range (16.5–19.5 µm), the average light trap reflectance is 0.028. For the other (shorter-wavelength) band-passes used in Fig. 4, the light trap reflectance averaged between 0.020 and 0.024. These small deviations from ideality, combined with the D25A precision discussed above, suggest that the overall uncertainties for our rock samples are of the order of 2% absolute emissivity, possibly increasing to 3–5% beyond ~18 µm. These uncertainties fall outside the resolution of the JWST instruments as discussed for specific precisions in the text, and all samples were analysed in a consistent manner. Furthermore, differences between samples in our set are consistent with features of the pure mineral spectra of their main components (for example, serpentine, plagioclase and amphibole; Supplementary Fig. 3). Therefore, the differences between samples measured here are considered robust. Although we did not examine how surface roughness affects spectra, variations in surface roughness do not change the spectral shape or feature location for basaltic rocks in any way that could be detected by JWST, and the largest emissivity difference expected between polished and rough surfaces for basaltic samples is 0.1 (ref. 36).

As a further demonstration of the reproducibility of our set-up, we analysed measurements taken 6–7 months apart using otherwise similar analytical conditions. For serpentine-rich sample TO01 (Supplementary Fig. 8), we considered as an example the two MIRI filters used in Fig. 4b to discern the presence of serpentine (F1800W and F770W). Using the same averaging method described above and averaging across the F1800W bandwidth, the TO01 samples differ by 0.39% relative. Across the F770W bandwidth, the TO01 samples differ by only 0.02% relative. For WB04 (Supplementary Fig. 9), we considered as an example the two MIRI filters used in Fig. 4c to differentiate Al_2O_3 contents (F1500W and F2100W). Averaging across the F1500W bandwidth, the WB04 samples differ by no more than 0.11% relative, and across the F2100W bandwidth, they differ by no more than 0.68% relative. One of the July 2021 spectra of WB04 (orange line in Supplementary Fig. 9) comprised fewer co-added scans: 72 as opposed to the 358 used for our final dataset. Even with fewer scans, the average emissivity values are within the ranges stated above. This figure also illustrates the noise reduction achieved by the addition of more scans.

Optical microscopy. Reflected light observations and images were acquired on a Leica DM2700P petrographic research microscope equipped with a Leica K5C camera and Leica Application Suite (LAS) X software, v.5.0.3.24880, at the Department of Earth and Atmospheric Sciences, Cornell University.

Bulk chemical composition. For all samples, the whole rock composition was determined by a standard XRF analysis of bulk powdered samples[60,61]. Fourteen samples were analysed before this study, although only nine were previously published (Supplementary Tables 1 and 2). Sample WB04 was analysed specifically for this study by the Hamilton Analytical Lab, Hamilton College, NY, in December 2021.

Raman mineralogy. Preliminary, qualitative work on all samples was performed to identify mineral phases and provide rough estimations of proportions, as a guide for subsequent analyses (for example, XRD). We used a WITec alpha300 R confocal Raman imaging microscope (Department of Earth and Atmospheric Sciences, Cornell University) equipped with a 532 nm laser, Control FIVE and Project FIVE software (v.5.3.12.104), and access to the RRUFF spectral database. Laser power was varied according to the material, and spot analyses were acquired at ×5 up to ×100 magnification. Manual signal optimization was performed by refocusing while running the oscilloscope. Several automated reflected light images and mosaics were acquired using focus stacking.

XRD mineralogy. Quantitative sample mineralogy was acquired by XRD using a Bruker D8 Advance ECO powder diffractometer at the Cornell Center for Materials Research. MDI JADE software (v.8.6), incorporating MDI Minerals and ICDD databases, was used for data reduction, peak fitting and whole pattern fitting. The main Raman-identified phases were selected manually to obtain the best data fits. The goodness of fit was defined as weighted (R)/expected (E) values, and all whole pattern fits had $R/E < 2$. Mineralogical data referenced herein use weight fractions (rather than volume fractions). This is more directly related to bulk (whole rock) composition and other commonly acquired parameters (for example, mineral chemistry). Weight and volume fraction mineralogy returned similar correlations with spectral variables (Supplementary Table 3). The estimated standard deviation for mineral abundances in each sample varied but was typically ≤3 wt% See the wpf.txt data sheets or Supplementary Table 3 for details.

Modelling

We modelled the thermally emitted planetary flux F_p from an exoplanet by assuming the surface to be entirely composed of each of the 15 rocks considered above. Our goal was to implement a quantitative yet accessible model in which laboratory emissivity data of rocks are quickly transformed into a theoretical exoplanet emission spectrum, which in turn is passed to PandExo to simulate JWST observations.

F_p/F_*. The thermally emitted planetary flux F_p from an exoplanet can be written as:

$$F_p = \left(\frac{R_p}{D}\right)^2 \int_{-\pi/2}^{\pi/2}\int_{-\pi/2}^{\pi/2} \epsilon_\lambda B_\lambda[T(\theta,\phi)]\cos^2\theta\cos\phi\,\mathrm{d}\theta\,\mathrm{d}\phi, \quad (1)$$

where R_p is the radius of the planet, D is the distance from us to the planet, ϵ_λ is the emissivity of the surface, B_λ is the black body radiance function, T is temperature, and θ is the latitude and ϕ is the longitude on the planet. By Kirchhoff's law, $\epsilon = 1 - r_h$, where r_h is the directional hemispherical reflectance, which we measured in the laboratory as described in previous sections. To implement a more straightforward model, we set aside the dependence of emissivity on emergence angle and used the acquired r_h as the single-input emissivity. If more detailed models are desirable for specific planetary targets and limited surface-type possibilities, a return to the Hapke framework or further laboratory data could reintroduce this variable. For the temperature T, a comprehensive dependence on latitude and longitude (θ, ϕ) can be evaluated by performing an energy balance calculation at each (θ, ϕ) grid point, as in ref. 12. Here, our models assume a constant temperature across the planet's hemisphere, which resulted in flux values that match the Spitzer 4.5 µm flux value for LHS 3844b (ref. 6). For example, in the LHS 3844b specific models, we chose the dayside average temperature of LHS 3844b observed by Spitzer (1,040 K)[6]. In our modelling approach, a heat redistribution factor of $f = 2/3$ (no atmosphere) is implicit.

Using $F_* = F_{inc}(D_p/D)^2$, where $F_{inc} = \pi I_\lambda (R_*/D_p)^2$, we can calculate F_p/F_*:

$$\frac{F_p}{F_*} = \left(\frac{R_p}{D_p}\right)^2 \left(\frac{\int_{-\pi/2}^{\pi/2}\int_{-\pi/2}^{\pi/2} \epsilon_\lambda B_\lambda[T(\theta,\phi)]\cos^2\theta\cos\phi\,\mathrm{d}\theta\,\mathrm{d}\phi}{\pi I_\lambda (R_*/D_p)^2}\right), \quad (2)$$

where R_* is the stellar radius, D_p is the distance between the star and the planet and I_λ is the stellar spectral radiance. For the models specific to LHS 3844 described in this work, we used a stellar spectrum model file for the star LHS 3844 from the PHOENIX database for theoretical stellar spectra[62]. These stellar model files are usually in units of janskys (spectral flux density). The spectral flux density F_λ is the integral of the spectral radiance I_λ over a hemisphere: $F_\lambda = \int I_\lambda \cos\theta\,\mathrm{d}\Omega = \pi I_\lambda$, where θ is the angle between the incoming radiation and the surface normal and $\mathrm{d}\Omega$ is the differential solid angle. As equation (2) uses the spectral radiance, we derived it by dividing the F_λ stellar models by π. Implicit in our modelling of a fixed-temperature planetary hemisphere is that all samples have the same bond albedo. This assumption is logical, as all samples are basaltic, and it is consistent with literature measurements of basaltic rocks, which show minimal scatter at optical wavelengths (for example, ref. 63). Ours is a conservative approach, as differences in bond albedo, and therefore planet temperature, would lead to offsets in the spectra at MIR wavelengths, which is the primary effect measured for LHS 3844b in ref. 6. Here, we focus on the information that can be gained directly from the overall shape and specific features of MIR basaltic planet spectra without also requiring direct measurements of their bond albedos at visible and near-infrared wavelengths.

JWST simulations. JWST observations with the MIRI LRS mode were simulated using PandExo[47]. We followed standard practice for time-series observations with JWST and assumed equal out-of-eclipse and in-eclipse times, plus another 1.0 h of the observational baseline to provide for a sufficiently large observation start time window and to allow for the treatment of the systemic effects of a 'ramp-like' detector. In total, this amounted to ×4 in-eclipse time. (The total transit and eclipse duration T_{14} of LHS 3844b is 31.3 min.)[64] We set a saturation limit of 100% and applied LHS 3844 stellar parameters obtained from the 2MASS catalogue[65]. PandExo used these parameters and a planetary emission model file (described above) to estimate the noise for a JWST MIRI LRS observation at a given spectral resolution and number of transits (or eclipses).

The photometric flux for various MIRI filters (Fig. 4) was estimated by performing trapezoidal integrations of the modelled planetary flux (F_p) for each sample, which were divided by trapezoidal integrations of the PHOENIX stellar flux of LHS 3844 (F_*) across the bandwidth for the stated filter, with spacing determined by the data point locations of the $R = 100$ flux model. Each planetary or stellar flux was multiplied by the corresponding wavelength and filter throughput before integration, following equation (1) in ref. 66. The integration was accomplished using the trapz function in MATLAB. Resultant filter fluxes match the expected value ranges based on Fig. 3. The display of these simulated MIRI filter data (Fig. 4) uses the perceptually uniform Batlow scientific colour palette[67], which is designed to reduce data distortion and be accessible for all readers[68].

Estimates for the precision of photometric observations with the MIRI broadband filter were generated using the JWST exposure time calculator (https://jwst.etc.stsci.edu/). MIRI imaging time-series calculations were performed for each of the nine filters (spanning ~5.6–25.5 µm) using the SUB256 subarray and FASTR1 read-out pattern. The number of groups per integration and the number of integrations per exposure were adjusted to maximize the signal-to-noise ratio (SNR) for the transit duration of LHS 3844b to just below the detector saturation limit. The SNR for a given filter was then used to estimate the precision of a single eclipse observation of the planet, which goes as 1/SNR.

Data availability

All data are available in the Supplementary Information and via Zenodo at https://doi.org/10.5281/zenodo.12822668 (ref. 69). Source data are provided with this paper.

Code availability

Code and explanations are found at: https://github.com/ishan-mishra/rocky_exo_jwst/tree/main.

References

1. Ehlmann, B. L. & Edwards, C. S. Mineralogy of the Martian surface. *Annu. Rev. Earth Planet. Sci.* **42**, 291–315 (2014).
2. Riu, L., Poulet, F., Bibring, J.-P. & Gondet, B. The M^3 project. 2. Global distributions of mafic mineral abundances on Mars. *Icarus* **322**, 31–53 (2019).
3. Rogers, A. D. & Christensen, P. R. Surface mineralogy of Martian low-albedo regions from MGS-TES data: implications for upper crustal evolution and surface alteration. *J. Geophys. Res.* **112**, E01003 (2007).
4. Lemelin, M. et al. The compositions of the lunar crust and upper mantle: spectral analysis of the inner rings of lunar impact basins. *Planet. Space Sci.* **165**, 230–243 (2019).
5. Nittler, L. R. et al. The major-element composition of Mercury's surface from MESSENGER X-ray spectrometry. *Science* **333**, 1847–1850 (2011).
6. Kreidberg, L. et al. Absence of a thick atmosphere on the terrestrial exoplanet LHS 3844b. *Nature* **573**, 87–90 (2019).
7. Greene, T. P. et al. Thermal emission from the Earth-sized exoplanet TRAPPIST-1 b using JWST. *Nature* **618**, 39–42 (2023).
8. Zieba, S. et al. No thick carbon dioxide atmosphere on the rocky exoplanet TRAPPIST-1 c. *Nature* **620**, 746–749 (2023).

9. Lammer, H. et al. The exosphere as a boundary: origin and evolution of airless bodies in the inner Solar System and beyond including planets with silicate atmospheres. *Space Sci. Rev.* **218**, 15 (2022).
10. Zahnle, K. J. & Catling, D. C. The cosmic shoreline: the evidence that escape determines which planets have atmospheres, and what this may mean for Proxima Centauri B. *Astrophys. J.* **843**, 122 (2017).
11. Crossfield, I. J. M. et al. GJ 1252b: a hot terrestrial super-Earth with no atmosphere. *Astrophys. J. Lett.* **937**, L17 (2022).
12. Hu, R., Ehlmann, B. L. & Seager, S. Theoretical spectra of terrestrial exoplanet surfaces. *Astrophys. J.* **752**, 7 (2012).
13. Burns, R. G. Crystal field spectra and evidence of cation ordering in olivine minerals. *Am. Mineral.* **55**, 1608–1632 (1970).
14. Ody, A. et al. Global investigation of olivine on Mars: insights into crust and mantle compositions. *J. Geophys. Res.: Planets* **118**, 234–262 (2013).
15. Hamilton, V. E. Thermal infrared (vibrational) spectroscopy of Mg-Fe olivines: a review and applications to determining the composition of planetary surfaces. *Geochemistry* **70**, 7–33 (2010).
16. Thomson, J. L. & Salisbury, J. W. The mid-infrared reflectance of mineral mixtures (7–14 μm). *Remote Sens. Environ.* **45**, 1–13 (1993).
17. Cooper, B. L. Midinfrared spectral features of rocks and their powders. *J. Geophys. Res.* **107**, 5017 (2002).
18. Herzberg, C. & O'Hara, M. Phase equilibrium constraints on the origin of basalts, picrites, and komatiites. *Earth-Sci. Rev.* **44**, 39–79 (1998).
19. Kushiro, I. & Kuno, H. Origin of primary basalt magmas and classification of basaltic rocks. *J. Petrol.* **4**, 75–89 (1963).
20. Le Maitre, R. W. et al. (eds) *Igneous Rocks: A Classification and Glossary of Terms* 2nd edn (Cambridge Univ. Press, 2002).
21. Putirka, K. D. & Rarick, J. C. The composition and mineralogy of rocky exoplanets: a survey of >4,000 stars from the Hypatia Catalog. *Am. Mineral.* **104**, 817–829 (2019).
22. Putirka, K. D. & Xu, S. Polluted white dwarfs reveal exotic mantle rock types on exoplanets in our solar neighborhood. *Nat. Commun.* **12**, 6168 (2021).
23. Madrigal, P. et al. A melt-focusing zone in the lithospheric mantle preserved in the Santa Elena ophiolite, Costa Rica. *Lithos* **230**, 189–205 (2015).
24. Zhang, Y., Gazel, E., Gaetani, G. A. & Klein, F. Serpentinite-derived slab fluids control the oxidation state of the subarc mantle. *Sci. Adv.* **7**, eabj2515 (2021).
25. Gazel, E. et al. Galapagos-OIB signature in southern Central America: mantle refertilization by arc-hot spot interaction. *Geochem. Geophys. Geosyst.* **10**, Q02S11 (2009).
26. Alfaro, A., Gazel, E., White, W. M., Jicha, B. & Rasbury, T. Unravelling the genesis of young continental-arc shoshonites in the Talamanca Cordillera, Costa Rica. *Lithos* **386–387**, 106017 (2021).
27. Gazel, E. et al. The record of the transition from an oceanic arc to a young continent in the Talamanca Cordillera. *Geochem. Geophys. Geosyst.* **20**, 2733–2752 (2019).
28. Valentine, G. A. et al. Lunar Crater volcanic field (Reveille and Pancake Ranges, Basin and Range Province, Nevada, USA). *Geosphere* **13**, 391–438 (2017).
29. Trela, J. et al. The hottest lavas of the Phanerozoic and the survival of deep Archaean reservoirs. *Nat. Geosci.* **10**, 451–456 (2017).
30. Aitken, B. G. & Echeverría, L. M. Petrology and geochemistry of komatiites and tholeiites from Gorgona Island, Colombia. *Contrib. Mineral. Petrol.* **86**, 94–105 (1984).
31. Ross, M. E. in *Petrology and Tectonic Significance of Mesozoic Mafic Dikes of the Coastal New England Igneous Province, Massachusetts*, Vol. 268 (eds Puffer, J. H. & Ragland, P. C.) 63–74 (Geological Society of America, 1992); https://pubs.geoscienceworld.org/books/book/407/chapter/3797920/
32. Whalen, W. T. *Geochemistry of Mafic Dikes from the Coastal New England Magmatic Province in Southeast Maine, USA and Nova Scotia, Canada*. Master's thesis, Virginia Polytechnic Institute and State Univ. (2019); http://hdl.handle.net/10919/90395
33. Christensen, P. R. et al. A thermal emission spectral library of rock-forming minerals. *J. Geophys. Res.* **105**, 9735–9739 (2000).
34. Donaldson Hanna, K. L. et al. Thermal infrared emissivity measurements under a simulated lunar environment: application to the Diviner Lunar Radiometer Experiment. *J. Geophys. Res.* **117**, E00H05 (2012).
35. Skulteti, A., Kereszturi, A., Szabo, M., Kereszty, Z. & Cipriani, F. Mid-infrared spectroscopic investigation of meteorites and perspectives for thermal infrared observations at the binary asteroid Didymos. *Planet. Space Sci.* **184**, 104855 (2020).
36. Rost, E., Hecker, C., Schodlok, M. & van der Meer, F. Rock sample surface preparation influences thermal infrared spectra. *Minerals* **8**, 475 (2018).
37. Le Bras, A. & Erard, S. Reflectance spectra of regolith analogs in the mid-infrared: effects of grain size. *Planet. Space Sci.* **51**, 281–294 (2003).
38. Biren, J. et al. High temperature spectral emissivity of glass and crystal-bearing basalts. *J. Volcanol. Geotherm. Res.* **430**, 107623 (2022).
39. Fortin, M.-A., Gazel, E., Kaltenegger, L. & Holycross, M. E. Volcanic exoplanet surfaces. *Mon. Not. R. Astron. Soc.* **516**, 4569–4575 (2022).
40. Lyon, R. J. P. Analysis of rocks by spectral infrared emission (8 to 25 microns). *Econ. Geol.* **60**, 715–736 (1965).
41. Schodlok, M. C., Green, A. & Huntington, J. A reference library of thermal infrared mineral reflectance spectra for the HyLogger-3 drill core logging system. *Aust. J. Earth Sci.* https://doi.org/10.1080/08120099.2016.1234508 (2016).
42. Hörz, F., Grieve, R., Heiken, G., Spudis, P. & Binder, A. in *Lunar Sourcebook, A User's Guide to the Moon* (eds Heiken, G. H. et al.) 61–120 (Cambridge Univ. Press, 1991).
43. Kite, E. S. & Barnett, M. N. Exoplanet secondary atmosphere loss and revival. *Proc. Natl Acad. Sci. USA* **117**, 18264–18271 (2020).
44. Ridden-Harper, A. et al. High-resolution transmission spectroscopy of the terrestrial exoplanet GJ 486b. *Astron. J.* **165**, 170 (2023).
45. Whittaker, E. A. et al. The detectability of rocky planet surface and atmosphere composition with the JWST: the case of LHS 3844b. *Astron. J.* **164**, 258 (2022).
46. Hapke, B. Bidirectional reflectance spectroscopy. 1. Theory. *J. Geophys. Res.* **86**, 3039–3054 (1981).
47. Batalha, N. E. et al. PandExo: a community tool for transiting exoplanet science with *JWST* & *HST*. *Publ. Astron. Soc. Pac.* **129**, 064501 (2017).
48. Winter, J. D. *Principles of Igneous and Metamorphic Petrology* 2nd edn (Prentice Hall, 2010).
49. Klein, F., Grozeva, N. G. & Seewald, J. S. Abiotic methane synthesis and serpentinization in olivine-hosted fluid inclusions. *Proc. Natl Acad. Sci. USA* **116**, 17666–17672 (2019).
50. Barstow, J. K. & Irwin, P. G. J. Habitable worlds with JWST: transit spectroscopy of the TRAPPIST-1 system. *Mon. Not. R. Astron. Soc. Lett.* **461**, L92–L96 (2016).
51. Patterson, S. N., Lynn, K. J., Prigent, C. & Warren, J. M. High temperature hydrothermal alteration and amphibole formation in Gakkel Ridge abyssal peridotites. *Lithos* **392–393**, 106107 (2021).
52. Poggiali, G. et al. Grain size effects on the infrared spectrum of mineral mixtures with dark components: new laboratory experiments to interpret low-albedo rocky planetary surfaces. *Astron. Astrophys.* **685**, A14 (2024).
53. Lee, J., Onstott, T. C., Cashman, K. V., Cumbest, R. J. & Johnson, D. Incremental heating of hornblende in vacuo: implications for $^{40}Ar/^{39}Ar$ geochronology and the interpretation of thermal histories. *Geology* **19**, 872 (1991).

54. Sautter, V., Jambon, A. & Boudouma, O. Cl-amphibole in the nakhlite MIL 03346: evidence for sediment contamination in a Martian meteorite. *Earth Planet. Sci. Lett.* **252**, 45–55 (2006).
55. Dobrică, E. & Brearley, A. J. Widespread hydrothermal alteration minerals in the fine-grained matrices of the Tieschitz unequilibrated ordinary chondrite. *Meteorit. Planet. Sci.* **49**, 1323–1349 (2014).
56. Evans, B. W. The serpentinite multisystem revisited: chrysotile is metastable. *Int. Geol. Rev.* **46**, 479–506 (2004).
57. Ehlmann, B. L., Mustard, J. F. & Murchie, S. L. Geologic setting of serpentine deposits on Mars. *Geophys. Res. Lett.* **37**, L06201 (2010).
58. Leask, E. K. & Ehlmann, B. L. Evidence for deposition of chloride on Mars from small-volume surface water events into the late Hesperian-early Amazonian. *AGU Adv.* **3**, e2021AV000534 (2022).
59. Blake, T. A. et al. Methods for quantitative infrared directional-hemispherical and diffuse reflectance measurements using an FTIR and a commercial integrating sphere. *Appl. Opt.* **57**, 432 (2018).
60. Johnson, D. M., Hooper, P. R. & Conrey, R. M. XRF analysis of rocks and minerals for major and trace elements on a single low dilution Li-tetraborate fused bead. *Adv. X-ray Anal.* **41**, 843–867 (1997).
61. Norrish, K. & Hutton, J. An accurate X-ray spectrographic method for the analysis of a wide range of geological samples. *Geochim. Cosmochim. Acta* **33**, 431–453 (1969).
62. Husser, T.-O. et al. A new extensive library of PHOENIX stellar atmospheres and synthetic spectra. *Astron. Astrophys.* **553**, A6 (2013).
63. Sgavetti, M., Pompilio, L. & Meli, S. Reflectance spectroscopy (0.3–2.5 µm) at various scales for bulk-rock identification. *Geosphere* **2**, 142 (2006).
64. Vanderspek, R. et al. TESS discovery of an ultra-short-period planet around the nearby M dwarf LHS 3844. *Astrophys. J. Lett.* **871**, L24 (2019).
65. Cutri, R. M. et al. VizieR Online Data Catalog: 2MASS all-sky catalog of point sources (Cutri+ 2003). *VizieR Online Data Catalog* **II**, 246 (2003); https://ui.adsabs.harvard.edu/abs/2003yCat.2246....0C
66. Charbonneau, D. et al. Detection of thermal emission from an extrasolar planet. *Astrophys. J.* **626**, 523–529 (2005).
67. Crameri, F. Scientific colour maps. *Zenodo* https://zenodo.org/records/8409685 (2023).
68. Crameri, F., Shephard, G. E. & Heron, P. J. The misuse of colour in science communication. *Nat. Commun.* **11**, 5444 (2020).
69. First, E. C., Mishra, I., Gazel, E., Lewis, N. K., Letai, J. & Hanssen, L. Supplementary materials for First et al. 2024 "Potential for observing geological diversity from mid-infrared spectra of rocky exoplanets." *Zenodo* https://doi.org/10.5281/zenodo.12822668 (2024).

Acknowledgements

We thank M. Fortin and M. Pfeifer for analytical training and J. Gustafson for assistance with sample preparation. E.C.F. is grateful to P. First (Georgia Tech) for helpful conversations regarding manuscript clarity and coding. This work made use of the Cornell Center for Materials Research Shared Facilities, which are supported through the NSF MRSEC programme (DMR-1719875). Our project also benefited from CRADA CN-21-01475 between NIST and Cornell. We thank the Heising-Simons Foundation for support through a 51 Pegasi b Fellowship (E.C.F.). E.G. acknowledges the Heising-Simons Foundation (Grant No. 2019-1498). I.M. was supported by the NASA FINESST programme (Grant No. 80NSSC20K1381). Certain equipment, instruments, software or materials, commercial or non-commercial, are identified in this paper to specify the experimental procedure adequately. Such identification is not intended to imply recommendation or endorsement of any product or service by NIST, nor is it intended to imply that the materials or equipment identified are necessarily the best available for the purpose.

Author contributions

E.C.F. selected samples, collected and analysed all geological data, calculated MIRI filter fluxes, and wrote the manuscript. I.M. wrote the astronomical modelling code and associated methods and was involved in many discussions and iterations of those items. E.G. developed and built the Cornell spectroscopy lab used in this research. E.G. and N.K.L. seeded the idea for this work and contributed significantly to data discussion and interpretation. E.G. and N.K.L. supervised the research groups within which this work took place. J.T.L. collected spectra and contributed to the discussion and editing of the manuscript. L.H. contributed guidance on and discussed the spectroscopic methods, supplied NIST reference samples and data, and contributed to manuscript edits.

Competing interests

The authors declare no competing interests.

Additional information

Supplementary information The online version contains supplementary material available at https://doi.org/10.1038/s41550-024-02412-7.

Correspondence and requests for materials should be addressed to Emily C. First or Esteban Gazel.

Peer review information *Nature Astronomy* thanks Daniel Koll and the other, anonymous, reviewer(s) for their contribution to the peer review of this work.